Institute for
Shock Physics
WASHINGTON STATE UNIVERSITY

"The role of micro-inertia on the shock structure in porous metals"

Z. Lovingera, C. Czarnotab, S. Ravindrana, A. Molinarib, G. Ravichandrana

DOI: 10.1016/j.jmps.2021.104508

Published: September 2021

Journal of the Mechanics and Physics of Solids

The role of micro-inertia on the shock structure in porous metals

Z. Lovinger[a,1], C. Czarnota[b], S. Ravindran[a], A. Molinari[b], G. Ravichandran[a]

[a]*Graduate Aerospace Laboratories, California Institute of Technology, 1200 E. California Blvd., Pasadena, CA 91125, USA*

[b] *Université de Lorraine – CNRS– Arts et Métiers ParisTech, LEM3, F-57000 Metz, France*

Abstract

The behavior of porous materials under shock loading is a multi-scale problem bridging orders of magnitude across the macroscale geometry and the microscale pores. Under static loading, this problem is well understood, relating mechanisms of pore closure and crushing to the equivalent macroscale models. The *dynamic* response of porous solids under shock loading is related to the effects of viscoplasticity and micro-acceleration fields around the void boundaries. The significance of the micro-inertia effects in modeling the dynamic behavior of porous materials remains an open question. In this work, an experimental investigation on closed-cell porous aluminum with small porosity provides the evidence for the first time of micro-inertia's fundamental role in describing the shock structure in these materials. Materials with different levels of porosity were manufactured using a modified process of additive manufacturing to achieve a mean pore size below 50μm. Plate impact experiments on porous aluminum samples were conducted at pressures in the range of 2 to 11 GPa. The structure of the steady shock was characterized as a function of porosity and shown to validate behavior revealed by an analytical approach (Czarnota et al. [J. Mech. Phys. Solids 107 (2017)]), highlighting the fundamental role of micro-inertia effects in such cases.

Keywords: Shock loading, Porous aluminum, Pore collapse, Micro-inertia

1. Introduction

Shock compression of porous metals is of current interest since these materials have the ability to mitigate impact and blast loadings [1-3]. At high shock amplitude, a significant part of energy can be absorbed by viscoplastic flow of the material after pore collapse is complete, resulting in dynamic regime of shock deformation [1]. Under moderate shock amplitude, as considered in this work, energy absorption is achieved mainly by large plastic deformations through pore collapse or crushing. The energy absorption and attenuation capabilities are of interest to many applications in protective technologies, for reducing peak shocks and accelerations, protecting sensitive electronics or system components [4]. Furthermore, many materials contain some level of porosity, as an inherent outcome of their manufacturing processes. As a consequence, much work has been done to characterize material response under shock loading, namely, measuring

[1] *Corresponding author: lovinger@caltech.edu*

and developing equations of state (EoS), which account for the influence of the initial porosity [5-6]. In the past decade, interest in the behavior of porous metals under shock loading has increased, as additive manufacturing (AM) of metals is becoming a desirable manufacturing technology also for shock applications. Current AM technologies introduce different levels of porosity, and their effects need to be explored, understood, and modeled properly. Much work can be found in the literature to model the behavior of porous materials, accounting for pore collapse mechanisms, beginning with the pioneering works of Hermann [7] and later of Carroll and Holt [8]. Viscous and micro-inertia effects, the latter being related to the local acceleration fields around the collapsing pore, were identified as the main mechanisms, affecting the behavior of the porous media, Fig. 1. In later years, the dominance and importance of these two factors have been examined using different approaches [9-12]. Nesterenko and co-workers have carried out much groundbreaking research on the dynamic compression of granular materials [13-14], incorporating porosity by the voids entrapped in-between the grains. While the dynamic compression of such materials has much in common with fully dense materials considered in the present work, they follow different deformation mechanisms, influenced by the finite size of the grains and associated porosity.

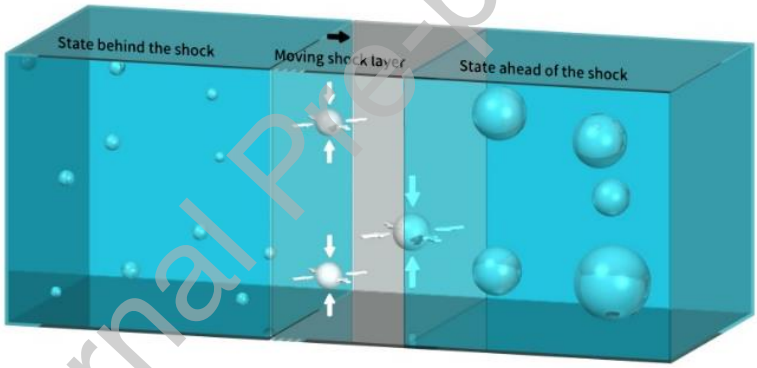

FIGURE 1. Steady shock wave propagating in a porous material and a schematic of the radial acceleration fields (micro-inertia effects) in the dynamic collapse of pores.

During the past two decades, Molinari and co-workers have developed several models, outlining the significance of micro-inertia to describe the shock structure of porous materials [15-17]. Recently, Czarnota et al. [18] demonstrated a comparison of an analytical model with experimental data, constructing the equation-of-state (EoS) for porous aluminum over a large range of porosities and shock levels. The comparison was shown to capture also a non-linear behavior when combining lower porosities and low shock intensities [18], and it converges to the fully dense material behavior as earlier developed by Molinari and Ravichandran [19]. The model outlined significant differences in the shock structure, if micro-inertia is accounted for or neglected. The current study was aimed to study these differences, seeking to examine the theoretical foundations in light of the experimental data, and to identify the conditions under which micro-inertia is a dominant factor.

An experimental campaign on porous aluminum alloy 6061 was carried out to examine the shock structure as a function of porosity and shock amplitude. The material with desired levels of porosity and pore size was manufactured using additive manufacturing (AM) technologies by altering the printing parameters. The experimental data was used to validate the effects of micro-inertia by comparison with predictions of the analytical model detailed in [18] and briefly described in this manuscript.

2. Plate impact experiments

2.1. Material: Porous aluminum

One of the main challenges in this work was to achieve a material with well characterized pores, enabling a fair comparison with an idealized material as assumed in the modeling. The specifications for the material were to achieve a homogeneous distribution of closed spherical pores, with an average diameter of 50 μm or less, regular in shape. The porous 6061 aluminum samples were made using Reactive Additive Manufacturing (RAM) technology (Elementum 3D, Erie, CO). The aluminum 6061 metal matrix composite, Al6061-RAM2, utilizes a fine dispersion of ceramic reinforcement particles (~2%) to act as heterogeneous grain nucleation sites and strengthening particles, to prevent the alloy from hot tearing during solidification. The average grain size of the aluminum alloy was 1-2μm. In order to achieve the desired characteristics for the porosity, the AM parameters, namely the hatch spacing and the laser velocity have been modified after scanning a large range of combinations. This custom designed AM process allowed reaching with these specifications, porosities in the range of 1%-8%. For the thicknesses of the samples and range of impact stresses, a steady shock was achieved for porosities up to 4%.

The porous aluminum samples were characterized using micro computed tomography (μCT). The scans were performed on match-stick type samples that were machined off the specimens, with a square cross-section of 2 mm by 2 mm, through the entire thickness of the sample. The small sized specimens allowed achieving a scanning resolution of ~3μm. Figure 2 shows two representative cross sections of an AM sample with 1.8% porosity, at approximately 1 mm from each end of the scanned sample. An edge detection function was used on the cross-section images to reveal the pore boundaries. At least 95% of the total volume of voids is constituted of voids with diameter in the range of 40-100 μm with a mean value of about 50 μm. Pore distribution was found to be homogeneous with mostly closed pores, regular in shape. A typical distribution for one of the tested specimens is shown in Fig.3.

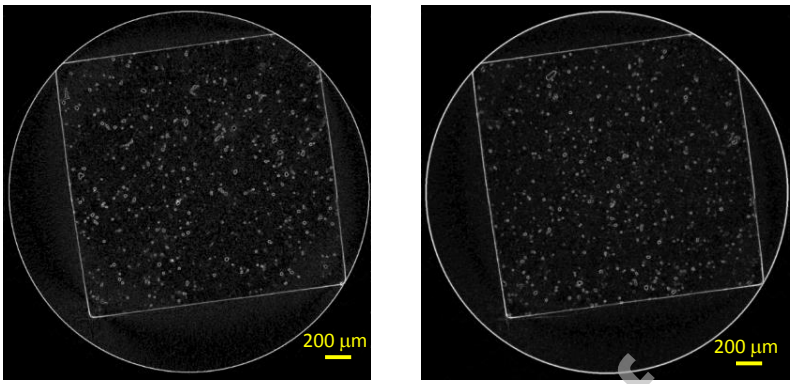

FIGURE 2 Cross sections from a MicroCT scan of an additively manufactured (AM) 6061 aluminum sample with 1.8% porosity: the images correspond to cross sections at ~ 1mm distance from each of the sample's ends, after the application of an edge detection function. The white edged boundaries outline the pores in the sample.

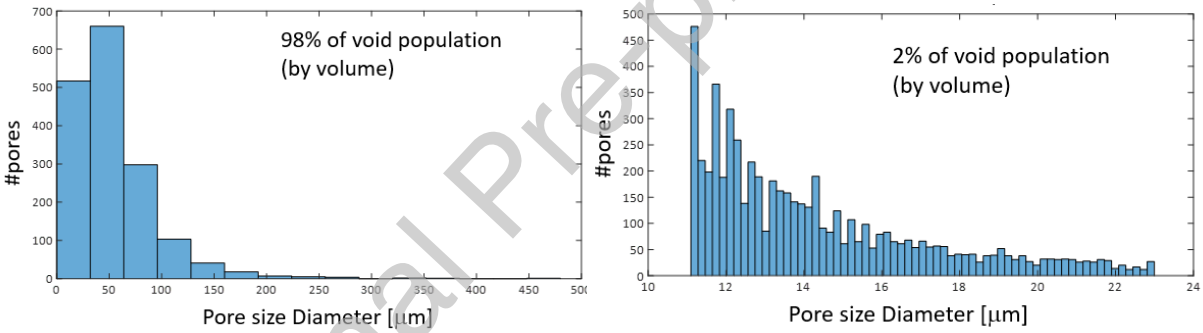

FIGURE 3 Pore size distribution for a specimen with 3% porosity, as determined from µCT scan.

2.2. Experimental set-up

Normal plate impact experiments were conducted using a 38.7 mm bore (1.525-inch) powder-gun facility in the Graduate Aerospace Laboratories at Caltech. Figure 4(a) shows a schematic of the experimental configuration of the plate impact experiments. The impactor was a 3mm steel plate, accelerated with a 76.2 mm (~3-inch) long polycarbonate sabot, and the aluminum target had a thickness of 10-12 mm. The geometry was designed to achieve both a steady compressive shock and a spall response. The spall response will not be analyzed in this paper. The main diagnostics was a continuous measurement of the free surface velocity, using Photonic Doppler Velocimetry (PDV) [20]. Figures 4(b) and 4(c) show the assembly of the target on the alignment gimbal and the focused PDV probe on the back surface.

FIGURE 4. Plate impact experimental set up: (a) schematic, (b) target assembly in the alignment gimbal and (c) PDV probe mounted on the back surface.

2.3. Results

Table 1 summarizes the experiments conducted in the present study. Four of the experiments were performed on dense samples – two of which were AM samples that were found to have some residual porosity, estimated to be less than 0.5% from the comparison shown later in Fig. 6. The other two were fully dense wrought Al6061 samples, which were used for comparison with a standard manufactured material. Experiments on six porous samples at two levels of porosity ~2% and ~4% were conducted. The actual calculated levels of porosity are shown in Table 1. The free surface velocity signals measured in the plate impact experiments are shown in Fig. 5.

TABLE 1. Experimental conditions of the plate impact experiments on aluminum with differing levels of porosity.

Experiment#	Porosity [%]	V_{impact} [m/s]	Thickness, *h* [mm]	Shock speed, *Us* [m/s]	Peak particle velocity, $v_{peak}=2u_p$ [m/s]	Shock stress [GPa]
PA1802	0.0 (W)*	467	11.87	5650	652±5	4.97±0.03
PA1803	0.0 res**	464	11.85	5490	642±13	4.79±0.07
PA1804	0.0 (W)*	985	11.89	6220	1377±10	11.56±0.14
PA1805	0.0 res**	988	11.85	6050	1355±26	11.12±0.07
PA1806	4.0	992	11.90	5290	1372±35	9.51±0.26
PA1901	1.8	998	11.90	5790	1401±73	10.87±0.58
PA1902	2.7	552	11.89	4680	760±50	4.72±0.32
PA1903	4.1	701	11.83	4610	890±30	5.37±0.19
PA1905	2.0	365	11.78	4230	438±15	2.48±0.09
PA1909	3.6	430	9.90	4170	595±35	3.26±0.20

* (W) – Denotes fully dense wrought material. All other materials were made using additive manufacturing (AM).
** AM samples, were manufactured to be fully dense samples with residual porosity of less than 0.5%.

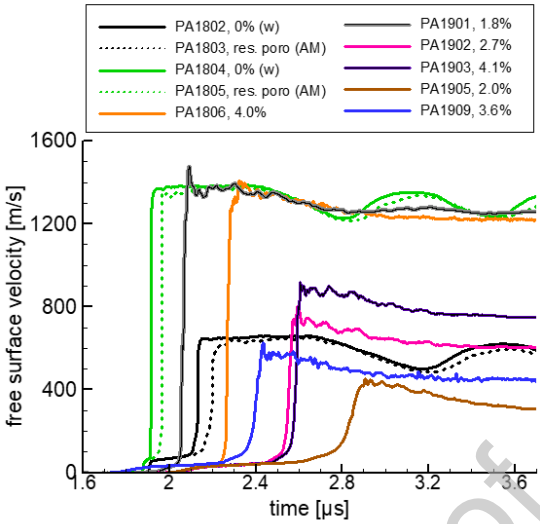

FIGURE 5. Measured free surface velocities in shock experiments on full dense and porous aluminum. The experimental parameters are shown in Table 1.

It can be seen that the wrought dense material and the AM material with small residual porosity show a similar behavior for the two shock levels, for both the plastic shock and spall signals, indicating very similar properties in the fully dense condition. The plastic shock speed of the AM material was slower by ~2%, which may be attributed to the low level of initial porosity (~0.5%). The plastic shock speed, U_S, and the peak free surface velocity, v_{peak}, equal to twice the maximum particle velocity, u_p, for each experiment are shown in Table 1. The range for v_{peak} and shock stress in Table 1 refers to experimental uncertainties (see Appendix A for more details).

3. Analytical model

The modeling of Czarnota et al. [18], which was used and demonstrated for porous aluminum, is considered in this paper and compared with the experimentally measured steady plastic shocks in aluminum specimens exhibiting various levels of initial porosities and of void sizes. This modeling is valid for uniaxial strain condition with monotonic compressive loading (void collapse), which corresponds to the framework analyzed in the present work. The approach considers uniaxial state of strain and relies partly on the use of the quasi-static compression curve (obtained for a given initial porosity f_0) combined with the chord criterion to obtain the Rayleigh line connecting state (+) to state (-), see Fig. 6. Both states are identified from a prescribed shock stress level σ^- or alternatively from shock speed U_s, or particle velocity at state (-) since a one to one correspondence exists between these variables [18].

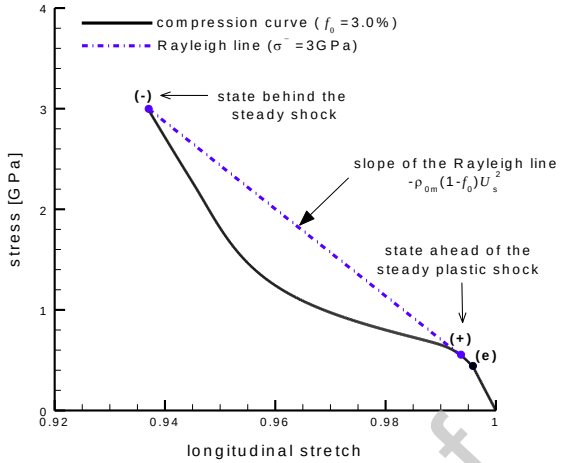

FIGURE 6 Compression curve for porous aluminum (f_0=3.0%) and Rayleigh line defining the shock path from state (+) to state (-) for a shock stress of 3 GPa, see Czarnota et al. [15]. The Rayleigh line, of slope $-\rho_{Om}(1-f_0)U_s^2$(ρ_{Om} being the matrix mass density) is tangent to the compression curve at state (+) and intersects this curve at state (-). From state (e), corresponding to the first plastic yielding, to state (+) ahead of the plastic shock, state variables are varying along the compression curve

3.1. Shock velocity vs. particle velocity

Let us consider a planar impact experiment of a porous metal sample initially at rest. Upon impact, first, an elastic wave is introduced in the specimen compressing the material particles from the initial state to state (e), corresponding to the first plastic yielding (Fig. 6). Then, depending on the shock stress level, a plastic wave fan may form, compressing material particles up to state (+). The plastic fan is followed by a plastic shock compressing furthermore, taking the material up to state (-), corresponding to the post shock state (e.g., Knowles [21], Faciu & Molinari [22] and Czarnota et al. [18]). Beyond a certain propagation distance, the plastic shock becomes steady, meaning that it travels with a constant shape at a constant shock speed U_s. Figure 6 illustrates the loci of states (e), (+) and (-) in the longitudinal stretch versus longitudinal (normal) stress diagram when a porous aluminum of initial porosity f_0=3.0% is submitted to a shock stress of 3 GPa. The corresponding shock velocity is deduced from the slope of the Rayleigh line. This approach has the advantage to infer, without the use of Hugoniot curves, a very good estimation of the relationship between the plastic shock velocity, U_s and the particle velocity, u_p at the rear of the shock (state (-)).

3.2. Shock structure

Once the states (+) and (-) are known, the shock structure can be determined from a nonlinear system of differential equations obtained using kinematic (uniaxial compression) and constitutive relationships (nonlinear elasticity, viscoplasticty, and micro-inertia). We recall here briefly the constitutive relationships describing micro-inertia effects and viscoplasticity. The reader can refer to Czarnota et al. [18, 23] for more details.

During the dynamic compaction process, the voids undergo a rapid collapse and material particles are subjected to very high acceleration in the vicinity of the cavities. The influence of those acceleration forces, developed at the microscale, is accounted for through the dynamic homogenization approach proposed by Molinari and Mercier [15] and developed for porous materials containing spherical voids (see Sartori et al. [24] and Subramani et al. [25] for an extension to spheroidal and cylindrical voids, respectively). In this work, the macroscopic Cauchy stress tensor $\boldsymbol{\Sigma}$ is the sum of two contributions:

$$\boldsymbol{\Sigma} = \boldsymbol{\Sigma}^{*} + \boldsymbol{\Sigma}^{\mathrm{dyn}} \tag{1}$$

where $\boldsymbol{\Sigma}^{\mathrm{dyn}}$ is the micro-inertia dependent part and $\boldsymbol{\Sigma}^{*}$is the micro-inertia independent contribution which includes the constitutive response of the matrix surrounding voids.

It is assumed that voids are keeping their spherical shape during the deformation process and that the dynamic stress is essentially spherical (valid for high stress triaxiality loadings, as it is the case for planar impacts). Under such considerations, only the mean stress is affected by micro-inertia and Eq. (1) reduces to:

$$\Sigma_m = \Sigma_m^{*} + \Sigma_m^{\mathrm{dyn}}, \boldsymbol{\Sigma}' = \boldsymbol{\Sigma}^{*\prime} \tag{2}$$

where $(\blacksquare)'$ is the deviatoric part of the 2nd order tensor ($\blacksquare$). The micro-inertia dependent Σ_m^{dyn} is expressed as,

$$\Sigma_m^{\mathrm{dyn}} = \rho_{Om} {a_0}^2 \left[\frac{f(1-f_0)}{f_0(1-f)}\right]^{1/3} \left[\dot{D}_m^p\left(f^{-1} - f^{-2/3}\right) + \left(D_m^p\right)^2\left(3f^{-1} - \frac{5}{2}f^{-\frac{2}{3}} - \frac{1}{2}f^{-2}\right)\right] \tag{3}$$

which corresponds to the model of Carroll and Holt [8]. ρ_{Om} is the initial matrix mass density, a_0 the initial void radius, f_0 and f stand for the initial and the current porosity, respectively. $D_m^p = \frac{1}{3}\mathrm{tr}(\boldsymbol{D}^p)$ is the mean part of the macroscopic plastic strain rate tensor $\boldsymbol{D}^p$(tr standing for the trace operator). A superimposed dot (.) denotes time derivative.

The micro-inertia independent part $\boldsymbol{\Sigma}^{*}$ is derived using the Gurson-Tvergaard-Needleman (GTN) model based viscoplastic flow surface (Gurson [26]; Tvergaard [27]; Needleman and Tvergaard [28]):

$$\Omega(\boldsymbol{\Sigma}^{*}, \overline{\sigma}, f) = \left(\frac{\Sigma_{\mathrm{eq}}^{*}}{\overline{\sigma}}\right)^2 + 2q_1 f \cosh\left(\frac{3}{2}q_2\frac{\Sigma_{\mathrm{m}}^{*}}{\overline{\sigma}}\right) - [1 + (q_1 f)^2] = 0 \tag{4}$$

with $q_1 = q_2 = 1$ parameters, $\Sigma_{\mathrm{m}}^{*} = \frac{1}{3}\mathrm{tr}(\boldsymbol{\Sigma}^{*})$ and $\Sigma_{\mathrm{eq}}^{*} = \sqrt{\frac{3}{2}\boldsymbol{\Sigma}^{*\prime}:\boldsymbol{\Sigma}^{*\prime}}$ (“tr” standing for the trace operator, “:” denoting the twice contracted product of second order tensors). $\overline{\sigma}$ is an average effective stress in the matrix.

Matrix viscous rate dependence is described by an overstress model in the form of a power-law relationship. In the present approach, the plastic shear strain rate Φ (assumed uniform) in the matrix is expressed as:

$$\Phi = (K_1 + K_2\gamma^p)\left(\frac{F_\sigma}{2T_1^*}\right)^M \tag{5}$$

where $F_\sigma = \bar{\sigma} - \sigma_a$ is the overstress and $\gamma^p = \int \Phi \mathrm{dt}$ is a measure of the plastic strain.

With this model, viscoplastic flow occurs when $F_\sigma > 0$, σ_a being the rate independent yield strength of the matrix. As in Clifton [29], we adopt a power law to describe strain hardening in the matrix:

$$\sigma_a = \sigma_{a0}\left[1 + \left(\frac{\gamma^p}{\gamma_0}\right)^{1/n}\right] \tag{6}$$

σ_{a0}, γ_0, n, K_1, K_2, M, and T_1^* are material parameters. The following numerical values of rate dependent parameters have been adopted: K_1=393s^{-1}, K_2=149.6, M =1.78, and T_1^*=1.6 MPa for rate dependent parameters and σ_{a0}=240MPa, γ_0=0.52, n=1.55 for strain hardening parameters. They correspond to material parameters for 6061-T6 aluminum which have been fitted by Clifton [29] and adopted in Molinari and Ravichandran [16] to describe the shock response of dense aluminum. It was shown in this last work that the rate sensitivity parameter M=1.78 (M=1/m represents the inverse of the strain rate exponent) is consistent with the 4th power law of Swegle and Grady [30].

It is worth noting, from Eq. (3), that micro-inertia effects are scaled by i) the mass density of the matrix and ii) the square of the initial void radius a_0, and iii) involves specific rate dependencies (linear dependence on $\dot{D}_m^p$ and quadratic influence of D_m^p) that are true signatures of micro-inertia also present for spheroidal and cylindrical voids, see Sartori et al. [24] and Subramani et al. [25].

The plastic shock layer width is a particular characteristic of steady shock waves, which was investigated using various descriptions of the shock structure. In Czarnota et al. [18,23], the shock structure was characterized by the variation of the accumulated plastic strain with respect to the moving coordinate. The corresponding shock width, defined to depict the width of the core of the shock, was found to be scaled by the initial void radius when micro-inertia effects are significant. Such situation is realized by increasing the shock amplitude or the initial void size. In the present work, the same matrix material as in Czarnota et al. [18] is considered (aluminum) and various configurations in terms of shock amplitudes and microstructures (pore sizes) are investigated. As an alternate to the approach of Czarnota et al. [18, 23], the shock structure here is characterized by the time variation of the free surface velocity to provide comparison with experimental results. As a consequence, a different definition is used for the shock layer width (see section 4.2).

Therefore, of central importance in the present modeling is the role played by micro-inertia effects in structuring the shock front. Usual damage models, such as the classical GTN model of porous plasticity (which is obtained when micro-inertia is neglected in the theory, i.e., no effect of the initial void radius, a_0) do not account for the rapid acceleration of material particles in the vicinity of collapsing voids. As illustrated in the forthcoming section 4.2, this family of micro-inertia independent models is not appropriate to describe the dynamic response of porous materials and is not able to capture the experimental wave profiles.

4. Comparison of experimental results with model predictions

4.1. EOS

Figure 7 shows the plots of shock velocity vs. particle velocity (U_s-u_p) predicted by the analytical modeling, with iso-shock pressure level contours shown as dotted lines. The data deduced from the current experiments are plotted as closed shaded circles for the AM samples and as shaded triangles for the wrought material targets. The comparison was found to be good for all the experimental points, including those in the non-linear regime at lower pressures. The range of variation (horizontal error bars), of the particle velocity behind the shock, is defined from minimum and maximum values corresponding to consecutive peaks and valleys observed in the free surface velocity profiles.

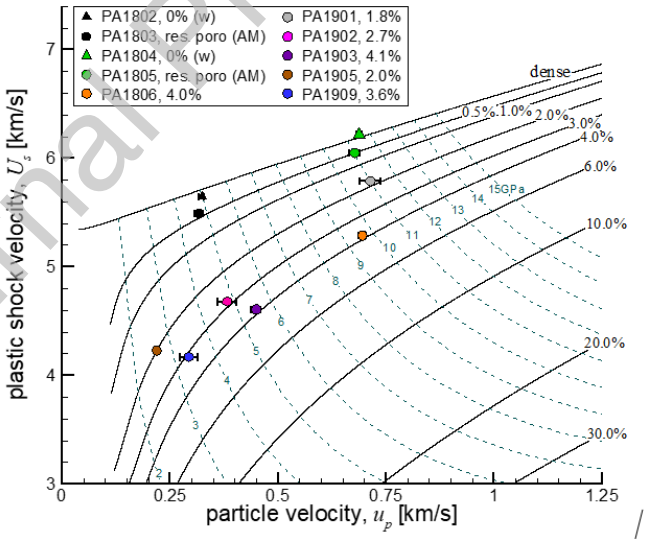

FIGURE 7. Shock velocity vs. particle velocity equation of state (U_s-u_p) diagram obtained from the analytical model [18] and measured data in solid filled circles for porous aluminum. Data for dense wrought materials are shown by triangles. The dotted lines plotted are iso-shock pressure levels in GPa.

A small discrepancy of ~2%, could be seen for the dense AM manufactured specimens with respect to the wrought Al6061 linear U_s-u_p relation for the fully dense materials. As mentioned earlier, this is a result of residual porosity in the AM samples due to the manufacturing process.

Indeed, it appears that the experimental results match well the predicted values by the analytical model when accounting for porosity in the vicinity of 0.5%.

Note that the porous model collapses to the earlier model presented in [19] for steady plastic shocks in dense aluminum, which was validated against experimental data of Johnson & Barker [31]. Further validation of plastic shockwave profiles measured in dense wrought (PA1802 and PA 1804) and near dense AM (PA1803 and PA1805) samples with the model developed in [19] is shown in Appendix B.

4.2. Shock width

The analytical model shows that when micro-inertia is dominant, the shock width is dependent on the pore size [18]. Furthermore, the shock width does not change significantly with increasing pressure for the same level of porosity, yet it shows broadening in the low-pressure range, where micro-inertia effects become small. In what follows, these observations from the modeling are examined through comparison with the experimentally measured shock width at different levels of porosity.

Using wave profiles (experimental and theoretical) the shock layer width is characterized in the present paper from the measured free surface velocity profile. More specifically, the shock width w is estimated from $\Delta t_{30/70}$ corresponding to the rise time where the free surface velocity is evolving from 30% of $\Delta v = v_{peak} - v^+$ to 70% of Δv, starting from v^+ (deduced from the analytical modeling), see Fig. 8. More specifically, the shock width is defined by:

$$w = U_s \Delta t_{30/70} \tag{7}$$

Note that the theoretical values of the plastic shock velocity U_s have been used for the model predictions of the shock width w, while measured values have been adopted for the experimental estimates. Note also that for experimental free surface velocity profiles reported in Fig. 5 and shown later in Figs. 10-11 solid lines are used to display data recorded in the range, $[v^+, v_{peak}]$.

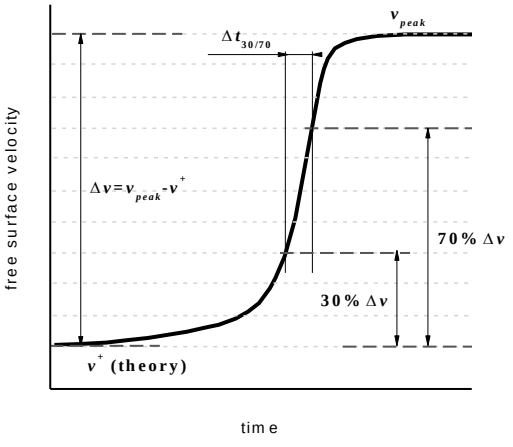

FIGURE 8 Schematic of the definition of the shock layer width according to Eq. (5).

Table 2 presents values of the particle velocities, v^+(deduced from the theory), v_{peak} (selected in the range of experimental uncertainties of Table 1), and of theoretical and experimental plastic shock speeds (U_s) used for calculation.

TABLE 2. Values of particle velocities, v^+(deduced from the theory), v_{peak} (determined from experiments), and of theoretical and experimental plastic shock speeds (U_s) used for calculation of the shock width in tested porous samples, see Eq. (7).

Experiment #	Porosity [%]	v_{peak} [m/s]	v^+ [m/s]	U_s (theo.) [m/s]	U_s(exp.) [m/s]
PA1806	4.0	1400	50.8	5265	5290
PA1901	1.8	1470	52.6	5825	5790
PA1902	2.7	808	54.8	4808	4680
PA1903	4.1	920	53.0	4574	4610
PA1905	2.0	452	77.8	4281	4230
PA1909	3.6	630	66.0	4125	4170

Figure 9 shows a comparison of the shock width as a function of the peak free-surface velocity, for two different levels of porosity. The porosities in the experimental samples varied from 1.8% to 4.1%. Comparison of the model predictions with experimental data are shown for four cases: (1) a fully dense material, (2) a porous material excluding micro-inertia effects, (3) a porous material with a pore radius of 20 μm, and (4) a porous material with a pore radius of 50 μm. Cases 3 and 4 including micro-inertia effects, correspond to the range of the measured pore sizes in the specimens. The experimental values of the shock width were calculated by multiplying the measured rise time by the plastic shock speed.

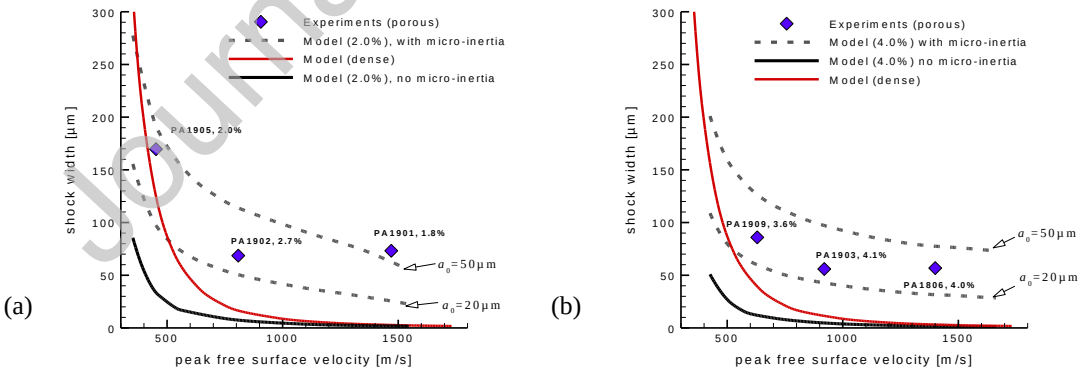

FIGURE 9. Shock width vs. peak free surface velocity for porosity levels of (a) 2% and (b) 4%: dashed lines correspond to theoretical results obtained for two initial void radii, a_0=20 and 50 μm. The solid black line corresponds to the micro-inertia independent case (no effect of pore radius) and the diamond symbols represent the experimental results. The solid red line represents the calculated case of a fully dense material.

From the data and comparison presented in Fig. 9 one could conclude the following: (1) significant differences are evident in the expected shock width, if micro-inertia is included or

excluded in the analytical model. When micro-inertia is *not accounted for*, the shock width decreases rapidly with increasing velocities and the corresponding shock pressures. Furthermore, the expected shock width is significantly small. Specifically, it could be noted that above a peak free surface velocity of 1000 m/s, the expected shock width when micro-inertia is excluded, is under 10 μm. Yet, when micro-inertia *is accounted for*, the shock width is expected to be 50-110 μm, for the range of measured pore sizes in the samples, a considerable factor of up to an order of magnitude in value. (2) The data points, measured over a large span of pressures/velocities, fit well in the range of shock widths predicted by the model when the micro-inertia effect is included. (3) The influence of increasing pressures is very different between the two cases. While for the case without micro-inertia, a strong decrease of the shock width is achieved, for the case when micro-inertia is dominant, the shock width shows a very mild decrease at relatively high impact velocities. Once again, the theoretical trend revealed when micro-inertia is included is well correlated with the experimental data, for both the levels of porosity.

In Figs. 10 and 11 a more detailed comparison of the predicted plastic shock profile is presented for the porous samples in the 4% porosity range and the 2% porosity range, respectively. The analytical model formulates the plastic response of the material, starting from its yield response, at the end of the elastic regime. Thus, the elastic precursor is not shown in these simulated profiles, and the calculated and compared responses focus on the evolution of the plastic shock. The experimentally measured profiles are compared with the model predictions when micro-inertia is excluded and for cases when micro-inertia is included, for the relevant range of pore sizes. It could be seen that the measured shock profiles lie well within this range of models with micro-inertia and it is very far from the sharp rise time predicted when micro-inertia is not considered.

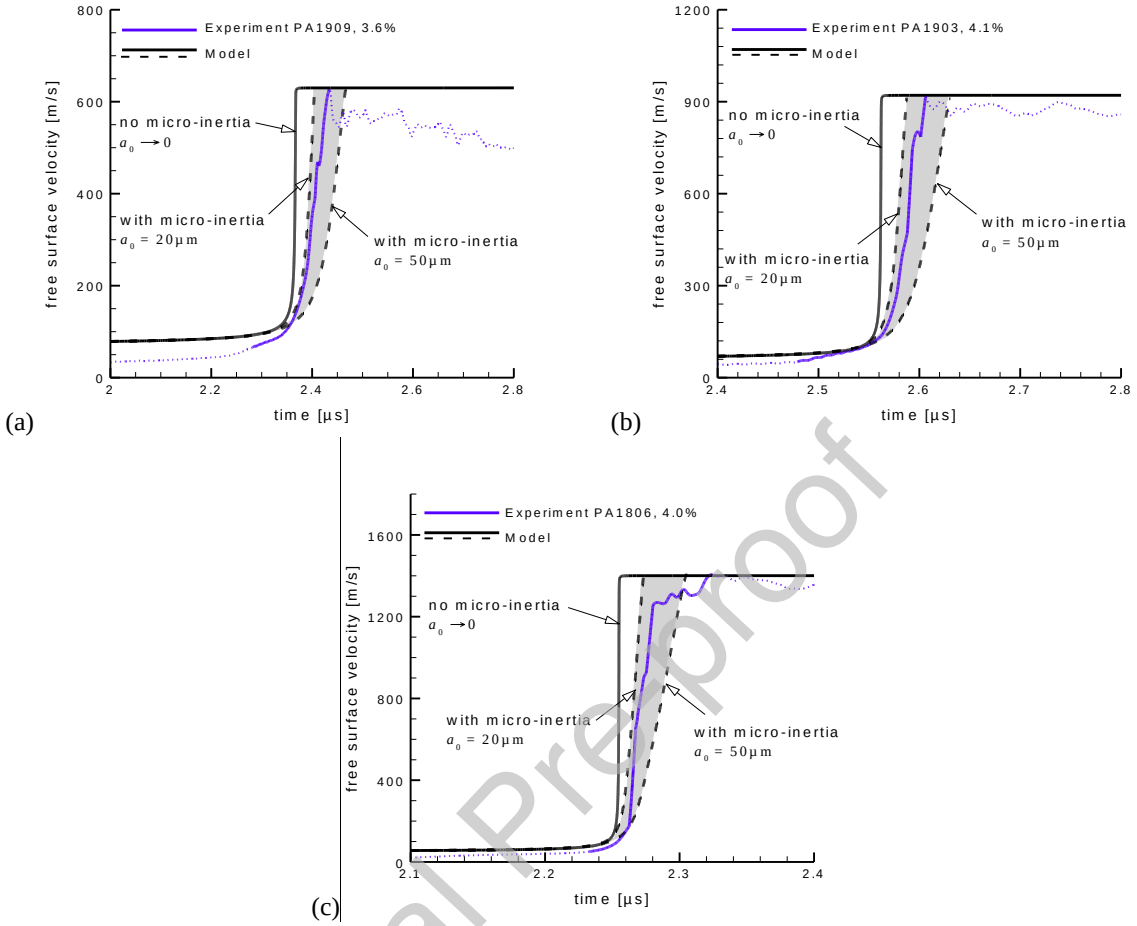

FIGURE 10. Plastic shock profiles for samples with ~4% porosity: comparison between the experimental shock profile and the prediction of the analytical model with no micro-inertia and with micro-inertia. The shaded area marks the plastic shock for a range of pore radii between 20 μm and 50 μm. Experimental curves are represented with solid blue lines in the range $[v^+, v_{peak}]$ and with thin dashed lines outside this range. The initial porosity considered in the modeling corresponds to those measured in the specimens: (a) 3.6%, (b) 4.1% and (c) 4%.

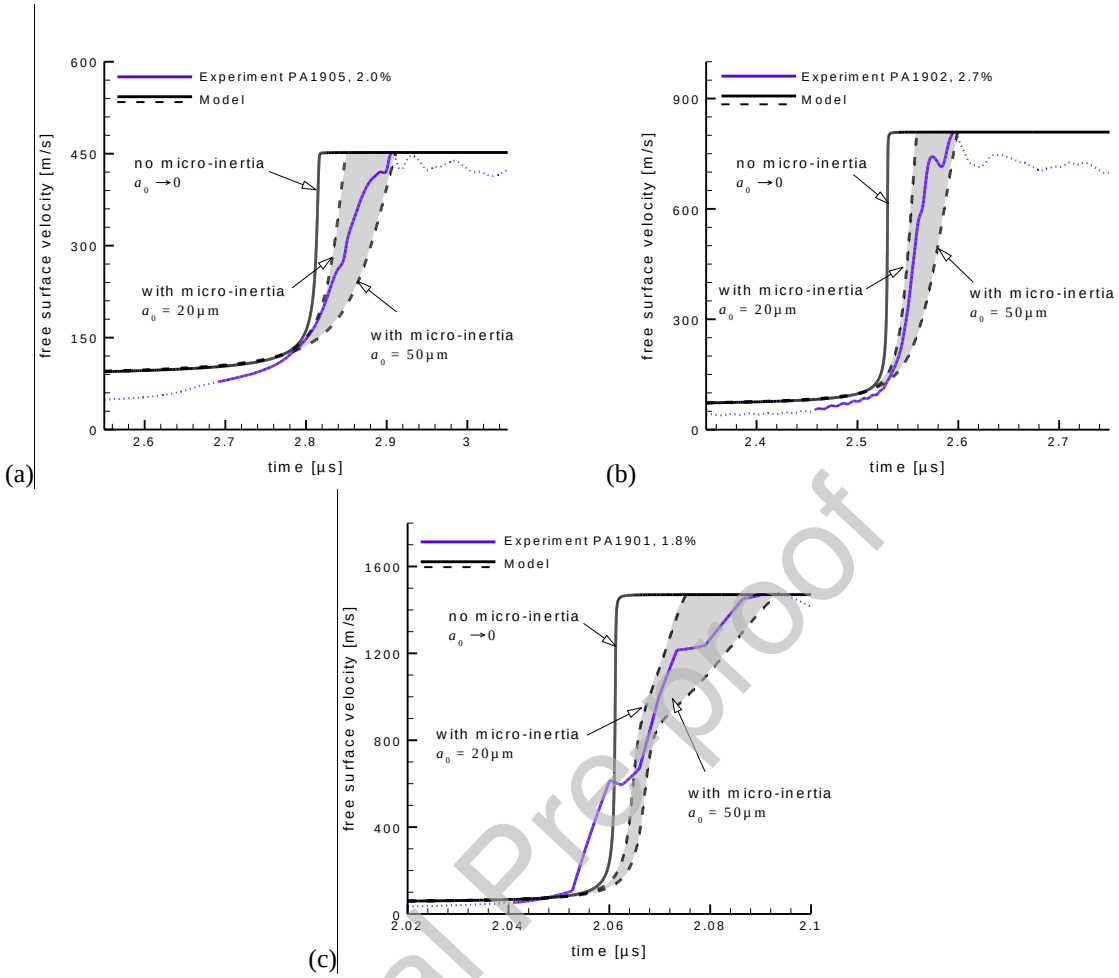

FIGURE 11 Plastic shock profiles for samples of porosity in the range, 1.8%-2.7%: comparison between the experimental shock profiles and the prediction of the analytical model with no micro-inertia and with micro-inertia. The shaded area marks the plastic shock for a range of initial pore radii (a_0) between 20 μm and 50 μm. Experimental curves are represented with solid blue lines in the range [v^+,v_{peak}] and with thin dashed lines outside this range. The initial porosity considered in the modeling corresponds to those measured in the specimens: (a) 2%, (b) 2.7% and (c) 1.8%.

One can note the peculiar behavior for the experiment PA1901 with porosity of 1.8% (Fig. 10(c)), where the shockwave profile predicted by the model (including micro-inertia) exhibits a dual wave structure. A net reduction in the rate of evolution of the velocity is observed above 900 m/s, while below, the evolution appears to be only slightly dependent on the void size. The measured shockwave also shows an apparent multiple stepped profile. In fact, it appeared from the modeling that the kinematics of the dynamic void collapse evolves from a quasi-frozen porosity mode (the porosity is only mildly evolving at the early stage) to a strong porosity evolution mode where plasticity is accumulated during the dynamic void closure process. This is highlighted in Figs. 10 and 11 where the difference between various models (with and without micro-inertia) becomes more marked when the free surface velocity reaches a sufficiently large

value (greater than 900 m/s). From the modeling, it appears that the dual wave structure is promoted when the porosity is low and the initial void size (a_0) is large.

5. Discussion of the robustness of the analysis

The comparison between theory and experiments presented above relies partly on the shock layer width, which may have some degree of arbitrariness. Other definitions can be proposed and the robustness of the results with regard to these definitions has to be checked.

In Fig. 8, the structure of the shock layer is characterized by the shock layer width, w defined by Eq. (7). Other characterizations of the shock layer width have also been examined:

$$w_{20/80} = U_s \Delta t_{20/80} \tag{8}$$

$$w_{40/60} = U_s \Delta t_{40/60} \tag{9}$$

where $\Delta t_{20/80}$ and $\Delta t_{40/60}$ are obtained in a similar manner as that depicted in Fig. 8. Among various characterizations considered in our work, $w_{40/60}$ appears as the lower bound estimate of the whole extent of the shock layer.

Figure 12 shows shock layer widths defined by Eqs. (8) and (9) vs. peak free surface velocity of samples for porosity levels of 2.0% (Fig. 12 (a), (c)) and 4.0% (Fig. 12 (b), (d)). One notes that experimental results fit the range of shock layer widths predicted by the model when micro-inertia is included. Thus, the comparison of experiments with theoretical results does not depend on the definition of the shock layer width.

Of peculiar behavior is a drastic drop in the shock layer width $w_{40/60}$ observed for a_0 = 50 μm in Fig. 12(a) when the particle velocity v_{peak} is larger than 1330m/s. This results from the dual shock structure that can occur at high shock stresses, which is depicted in the shockwave profile of Fig. 10(c). In fact, $w_{40/60}$ is characterizing a part of the shock layer where the variation in velocity is in the range ~620 m/s to 900 m/s, thus covering mainly the first part of the shockwave profile where the structure is evolving rapidly, see Fig. 11(c). Recall that this first part of the dual structure is less dependent on the void size. Since the shock widths, $w_{60/80}$ and $w_{30/70}$ are covering a larger extent of the wave structure (including the two parts of the dual structure), the sudden decrease in shock layer width at high velocity is not so pronounced (see Fig. 8 and Fig. 12(b)).

Hence, one can surmise that immaterial of the adopted characterization of the shock layer width (Eqs. (5)-(7)), the experimental data is in good agreement with the model predictions when micro-inertia effects are included. It is recognized that a single parameter (the shock layer width) may be not sufficient to characterize the shockwave structure and that a comparison analysis cannot rely on this unique measure. The close agreement between theoretical and experimental shockwave profiles (Figs. 10 and 11) provides additional evidence of the fundamental role of micro-inertia in structuring shockwaves in porous metals.

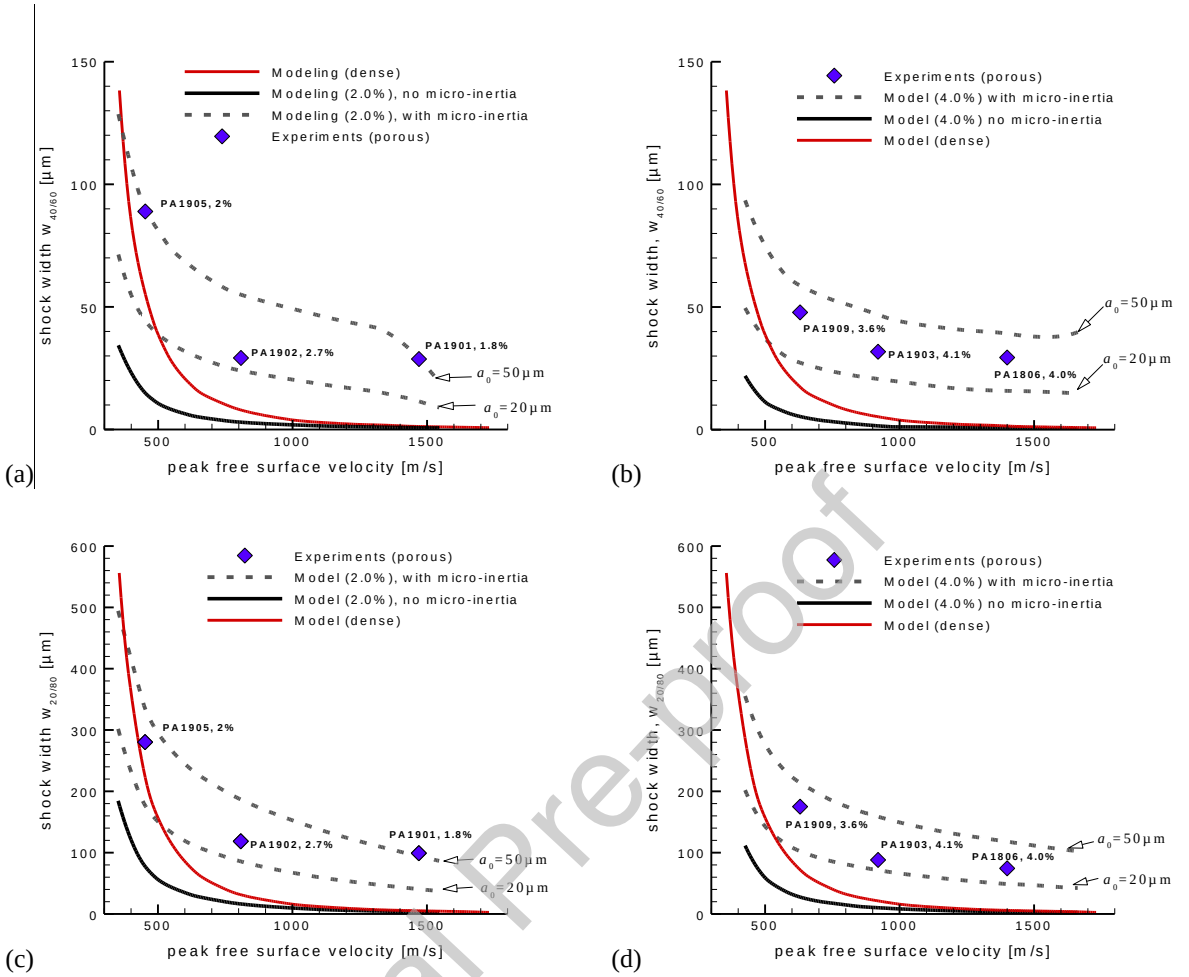

FIGURE 12 Shock layer widths $w_{40/60}$ (a, b) and $w_{20/80}$ (c, d) versus peak free surface velocity v_{peak} for samples of porosity in the range, 1.8%-2.7% (a, c) and of ~4% porosity (b, d). Dashed lines are theoretical results obtained for two initial void radii a_0 = 20 and 50μm, solid black lines are the micro-inertia independent cases (no effect of pore radius, a_0) and the diamond symbols correspond to the experimental results. The solid red lines represent the theoretical predictions for a fully dense material.

6. Summary and conclusion

A series of plate impact shock experiments was conducted on 6061 aluminum samples with porosities of 0-4% to examine the effect of porosity on shock structure, at shock pressures of 2-11 GPa. The materials were additively manufactured using AM technology with modified printing parameters to achieve an average pore radius of ~25μm. The experimentally measured shock widths in the wide span of shock amplitude-porosity conditions were compared with a recently developed analytical model incorporating micro-inertia. The experimental investigation provides for the first time evidence of the fundamental role of micro-inertia effects to describe the shock structure in porous solids. The analytical model predictions capture well the experimentally measured response. The shock velocity vs. particle velocity (U_s-u_p) results were found to correlate well with the analytical prediction, including those in the non-linear regime of low porosities and low pressures. The experimental data obtained over a large span of pressures/velocities, agree well with the range of shock widths predicted by the model in reference of the actual pore sizes, when the micro-inertia effect is included. Overall, this work

establishes clearly the role of micro-inertia in modeling dynamic response of porous materials and the large possible discrepancies or errors when it is excluded.

Acknowledgment

C. Czarnota and A. Molinari gratefully acknowledge the financial support of the French National Research Agency ANR (LabEx DAMAS, 535 Grant No. ANR-11-LABX-0008-01). G. Ravichandran acknowledges the support of the U.S. Department of Energy, DOE/NNSA (Award Nos. DE-NA0002007, DE-NA0003957). The authors would like to acknowledge the work of Jacob Nuechteriein and Adam J. Polizzi from Elementum 3D for the design and manufacturing of the AM materials used in this work. The authors would like to thank Dr. Branden Kappes and Professor Aaron Stebner from the Colorado School of Mines for conducting micro-tomography on the porous samples.

Declaration of interests

The authors declare that they have no known competing financial interests or personal relationships that could have appeared to influence the work reported in this paper.

REFERENCES

[1] Nesterenko VF. (2001) Dynamics of heterogeneous materials, Springer-Verlag, New York. https://doi.org/10.1007/978-1-4757-3524-6

[2] Smith PD & Hetherington JG. (1994) Blast and Ballistic Loading of structures, Butterworth-Heinemann Ltd., Oxford. https://doi.org/10.1201/9781482269277

[3] Goel, MD., Altenhofer P., Matsagar VA, Gupta AK, Mundt C. & Marburg S. (2015) Interaction of a shock wave with a closed cell aluminum metal foam. Combust Explos Shock Waves 51**,** 373–380. https://doi.org/10.1134/S0010508215030144.

[4] Li, B., Zhao G. & Lu T. (2012) Low strain rate compressive behavior of high porosity closed-cell aluminum foams. Sci. China Technol. Sci. 55**,** 451–463. https://doi.org/10.1007/s11431-011-4685-5.

[5] Medvedev AB & Trunin RF (2012) Shock compression of porous metals and silicates, Physics-Uspekhi 55, 773–789.https://doi.org/10.3367/UFNe.0182.201208b.0829

[6] McQueen RG., Marsh SP, Taylor JW, Fritz JN & Carter WJ (1970), High-Velocity Impact Phenomena, ed. by Kinslow R, Academic Press, New York, 244.

[7] Hermann W (1969) Constitutive Equation for the Dynamic Compaction of Ductile Porous Materials, J. Appl. Phys. 40, 2490-2499. https://doi.org/10.1063/1.1658021.

[8] Carroll MM & Holt AC (1972) Static and dynamic pore collapse relations for ductile porous materials, J. Appl. Phys. 43, 1626-1636. https://doi.org/10.1063/1.1661372

[9] Johnson JN (1981) Dynamic fracture and spallation in ductile solids, J. Appl. Phys. 52, 2812-2825. https://doi.org/10.1063/1.329011

[10] Ortiz M. & Molinari A. (1992) Effect of strain hardening and rate sensitivity on the dynamic growth of a void in a plastic material, J. Appl. Mech. 114, 48–53. https://doi.org/10.1115/1.2899463

[11] Cohen, T. & Durban, D. (2015) Steady shock waves in porous plastic solids, Int. J. Solids Struct. 71, 70–78. https://doi.org/10.1016/j.ijsolstr.2015.06.002

[12] Carroll MM., Kim KT. & Nesterenko VF. (1986) The effect of temperature on viscoplastic pore collapse. J. Appl. Phys. 59, 1962–1967. https://doi.org/10.1063/1.336426

[13] Nesterenko VF. & Lazaridi AN (1990) Regimes of shock-wave compaction of granular materials, High pressure research, 5, 835-837. https://doi.org/10.1080/08957959008246273

[14] Benson DJ., Nesterenko VF., Jonsdottir F. & Meyers MA. (1997) Quasistatic and dynamic regimes of granular material deformation under impulse loading, J. Mech. Phys. solids 45, 1955–1999. https://doi.org/10.1016/S0022-5096(97)00021-5

[15] Molinari, A. & Mercier, S. (2001) Micromechanical modelling of porous materials under dynamic loading. J. Mech. Phys. Solids 49, 1497–1516. https://doi.org/10.1016/S0022-5096(01)00003-5

[16] Czarnota C., Jacques N., Mercier S. & Molinari A. (2008) Modelling of dynamic ductile fracture and application to the simulation of plate impact tests on tantalum, J. Mech. Phys. Solids 56, 1624–1650. https://doi.org/10.1016/j.jmps.2007.07.017

[17] Jacques N., Czarnota C., Mercier S. & Molinari A. (2010) A micromechanical constitutive model for dynamic damage and fracture of ductile materials, Int. J. Fract. 162, 159–175. https://doi.org/10.1007/s10704-009-9436-2

[18] Czarnota C., Molinari A. & Mercier S. (2017) The structure of steady shock waves in porous metals, J. Mech. Phys. Solids, 107, 204-228. https://doi.org/10.1016/j.jmps.2017.06.005

[19] Molinari, A. & Ravichandran, G. (2004) Fundamental structure of steady plastic shock waves in metals. *J. Appl. Phys., 95,* 1718 – 1732. https://doi.org/10.1063/1.1640452

[20] Dolan DH (2010) Accuracy and precision in photonic Doppler velocimetry, Rev. Sci. Instrum. 81, 053905. https://doi.org/10.1063/1.3429257

[21] Knowles, J.K. (2002). Impact-induced tensile waves in a rubberlike material. J. Appl. Math. 62, 1153–1175. https://doi.org/10.1137/S0036139901388234

[22] Fãciu, C. & Molinari, A. (2006). On the longitudinal impact of two phase transforming bars. Elastic versus a rate-type approach. Part I: the elastic case. Int. J. Solids Struct., 43, 497–522. https://doi.org/10.1016/j.ijsolstr.2005.06.023

[23] Czarnota C., Molinari & Mercier S. (2020) Steady shock waves in porous metals: Viscosity and micro-inertia effects, Int. J. Plast., 135, 102816. https://doi.org/10.1016/j.ijplas.2020.102816

[24] Sartori, C., Mercier, S., Jacques, N. & Molinari, A. (2015). Constitutive behavior of porous ductile materials accounting for micro-inertia and void shape. Mech. Mater. 80, 324–339. https://doi.org/10.1016/j.mechmat.2013.12.006

[25] Subramani, M., Czarnota, C., Mercier, S. & Molinari, A. (2020). Dynamic response of ductile materials containing cylindrical voids. Int. J. Fract. 222, 197–218. https://doi.org/10.1007/s10704-020-00441-7

[26] Gurson, A.L. (1977). Continuum theory of ductile rupture by void nucleation and growth: Part I - yield criteria and flow rules for porous ductile media. J. Eng. Mater. Technol. 99, 2–15. https://doi.org/10.1115/1.3443401

[27] Tvergaard, V. (1981). Influence of voids on shear bands instabilities under plane strain conditions. Int. J. Fract. 17, 389–407. https://doi.org/10.1007/BF00036191

[28] Needleman, A., Tvergaard, V., 1991. An analysis of dynamic, ductile crack growth in a double edge cracked specimen. Int. J. Fract. 49, 41–67. https://doi.org/10.1007/BF00013502

[29] Clifton, R.J., 1971. On the analysis of elastic/visco-plastic waves of finite uniaxial strain. In: Burke, J.J., Weiss, V. (Eds.), Shock Waves and the Mechanical Properties of Solids. Syracuse University Press, pp. 73–119.

[30] Swegle, J.W.& Grady, D.E. (1985). Shock viscosity and the prediction of shock wave rise times. J. Appl. Phys. 58, 692–701. https://doi.org/10.1063/1.336184

[31] Johnson J. N., & Barker L. M. (1969). Dislocation Dynamics and Steady Plastic Wave Profiles in 6061- T6 Aluminum. J. Appl. Phys. 40, 4321. https://doi.org/10.1063/1.1657194

Appendix A- uncertainties on measured variables

Uncertainties were calculated for the presented data of shock and particle velocities U_s and u_p. These are shown as error bars in Figure 7.

- The uncertainty in the actual measured signal of u_p is related to the sampling rate of the digital channels that were used for the measurement of the time of contact on the tilt pins (2GHz→0.5ns). Maximum error would be 2ns.
- The range of variation, of the particle velocity behind the shock u_p, is defined from minimum and maximum values corresponding to consecutive peaks and valleys observed in the free surface velocity profiles.
- The uncertainties on U_s are calculated as the ratio between target thickness and the plastic shock speed. Target thickness was measured to an accuracy of 0.01 mm and u_p as explained above. The calculated uncertainty of the value of U_s is 0.01 mm/μs (rounded to smallest error of 10 m/s).
- Uncertainties on normal stress σ_x, are calculated by the corresponding relation of: $\sigma_x=\rho U_s u_p$, accounting for uncertainties in the density ρ (measurement uncertainty is 0.01 g/cm^3), the shock speed U_s and particle velocity, u_p.

Appendix B- Comparison of experimental results with model predictions for fully dense aluminum

Figure 13 compares the experimental shockwave profiles in dense samples (PA1802 to PA1805, see Table 1), with results obtained from the analytical approach of Molinari & Ravichandran [16]. It could be seen that experimental results are well reproduced by the model predictions. The small discrepancy, observed for PA1803 (Fig. 13c) and PA1805 (Fig. 13d), can be explained by the additive manufacturing process, which resulted in residual porosity in the samples used in these experiments.

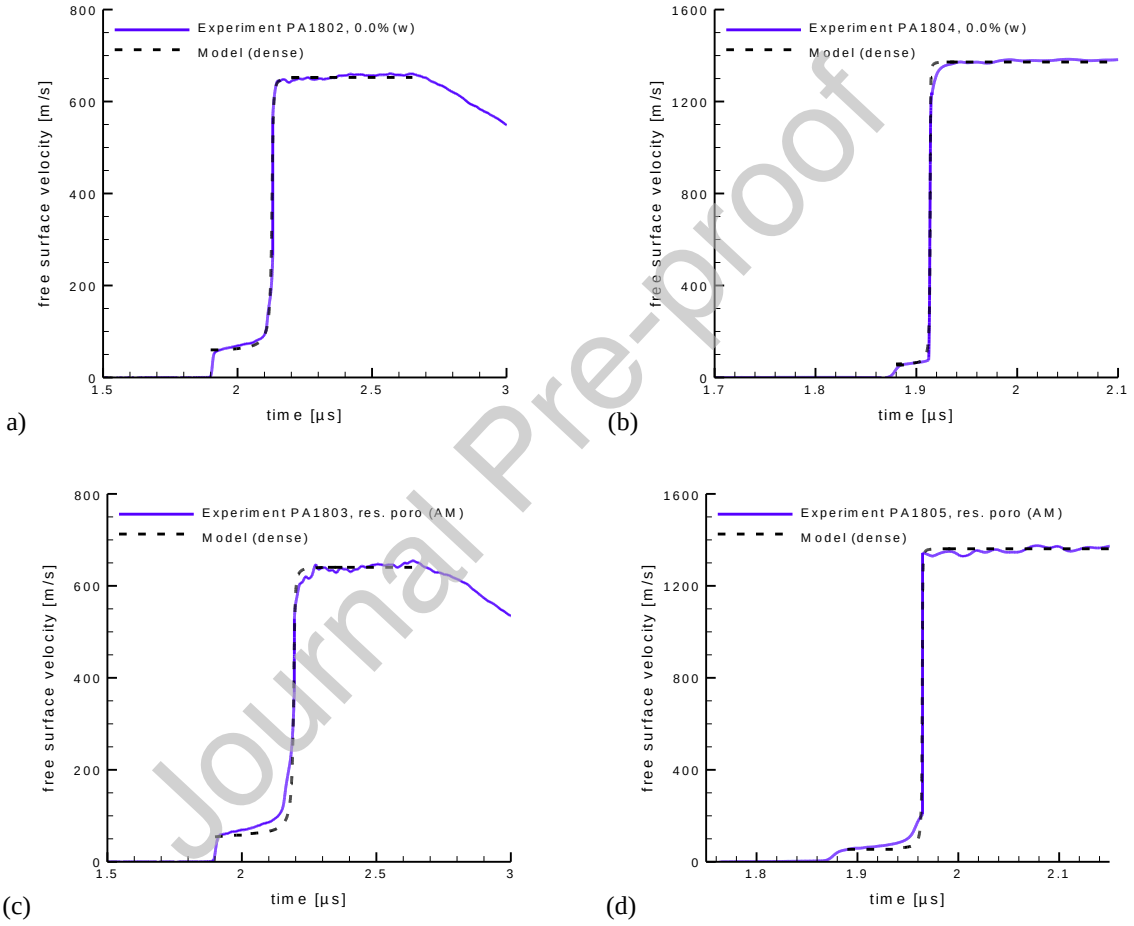

FIGURE 13 Comparison of experimental and analytical model [16] for plastic shock profiles. Dense or near dense aluminum samples are considered: (a, b) fully dense wrought Al6061 samples impacted at V_{impact}=467m/s and 985m/s, respectively and (c, d) AM samples with residual porosity of ~0.5% impacted at V_{impact} =465 and 988m/s, respectively, see Table 1.